Search for relativistic fractionally charged particles in space

F. Alemanno,[1,2] C. Altomare,[3] Q. An,[4,5] P. Azzarello,[6] F. C. T. Barbato,[1,2] P. Bernardini,[7,8] X. J. Bi,[9,10] M. S. Cai,[11,12] E. Casilli,[7,8] E. Catanzani,[13] J. Chang,[11,12] D. Y. Chen,[11] J. L. Chen,[14] Z. F. Chen,[11,12] M. Y. Cui,[11] T. S. Cui,[15] Y. X. Cui,[11,12] H. T. Dai,[4,5] A. De Benedittis,[7,8,†] I. De Mitri,[1,2] F. de Palma,[7,8] M. Deliyergiyev,[6] A. Di Giovanni,[1,2] M. Di Santo,[1,2] Q. Ding,[11,12] T. K. Dong,[11] Z. X. Dong,[15] G. Donvito,[3] D. Droz,[6] J. L. Duan,[14] K. K. Duan,[11] D. D'Urso,[13,‡] R. R. Fan,[10] Y. Z. Fan,[11,12] F. Fang,[14] K. Fang,[10] C. Q. Feng,[4,5] L. Feng,[11] M. F. Alonso,[1,2] J. M. Frieden,[1,2,§] P. Fusco,[3,16] M. Gao,[10] F. Gargano,[3] K. Gong,[10] Y. Z. Gong,[11] D. Y. Guo,[10] J. H. Guo,[11,12] S. X. Han,[15] Y. M. Hu,[11] G. S. Huang,[4,5] X. Y. Huang,[11,12] Y. Y. Huang,[11] M. Ionica,[13] L. Y. Jiang,[11] W. Jiang,[11] J. Kong,[14] A. Kotenko,[6] D. Kyratzis,[1,2] S. J. Lei,[11] W. L. Li,[15] W. H. Li,[11,12] X. Li,[11,12] X. Q. Li,[15] Y. M. Liang,[15] C. M. Liu,[4,5] H. Liu,[11] J. Liu,[14] S. B. Liu,[4,5] Y. Liu,[11] F. Loparco,[3,16] C. N. Luo,[11,12] M. Ma,[15] P. X. Ma,[11] T. Ma,[11] X. Y. Ma,[15] G. Marsella,[7,8,‖] M. N. Mazziotta,[3] D. Mo,[14] M. M. Salinas,[6] X. Y. Niu,[14] X. Pan,[11,12] A. Parenti,[1,2] W. X. Peng,[10] X. Y. Peng,[11] C. Perrina,[6,§] R. Qiao,[10] J. N. Rao,[15] A. Ruina,[6] Z. Shangguan,[15] W. H. Shen,[15] Z. Q. Shen,[11] Z. T. Shen,[4,5] L. Silveri,[1,2] J. X. Song,[15] M. Stolpovskiy,[6] H. Su,[14] M. Su,[17] H. R. Sun,[4,5] Z. Y. Sun,[14] A. Surdo,[8] X. J. Teng,[15] A. Tykhonov,[6] J. Z. Wang,[10] L. G. Wang,[15] S. Wang,[11] S. X. Wang,[11,12] X. L. Wang,[4,5] Y. Wang,[4,5] Y. F. Wang,[4,5] Y. Z. Wang,[11] D. M. Wei,[11,12] J. J. Wei,[11] Y. F. Wei,[4,5] D. Wu,[10] J. Wu,[11,12] L. B. Wu,[1,2] S. S. Wu,[15] X. Wu,[6] Z. Q. Xia,[11] E. H. Xu,[4,5] H. T. Xu,[15] J. Xu,[11] Z. H. Xu,[11,12] Z. L. Xu,[11] Z. Z. Xu,[4,5] G. F. Xue,[15] H. B. Yang,[14] P. Yang,[14] Y. Q. Yang,[14] H. J. Yao,[14] Y. H. Yu,[14] G. W. Yuan,[11,12] Q. Yuan,[11,12] C. Yue,[11] J. J. Zang,[11,¶] S. X. Zhang,[14] W. Z. Zhang,[15] Yan Zhang,[11] Yi. Zhang,[11,12] Y. J. Zhang,[14] Y. L. Zhang,[4,5] Y. P. Zhang,[14] Y. Q. Zhang,[11] Z. Zhang,[11] Z. Y. Zhang,[4,5] C. Zhao,[4,5] H. Y. Zhao,[14] X. F. Zhao,[15] C. Y. Zhou,[15] and Y. Zhu[15]

(DAMPE Collaboration)[*]

[1]*Gran Sasso Science Institute (GSSI), Via Iacobucci 2, I-67100 L'Aquila, Italy*
[2]*Istituto Nazionale di Fisica Nucleare (INFN)—Laboratori Nazionali del Gran Sasso, I-67100 Assergi, L'Aquila, Italy*
[3]*Istituto Nazionale di Fisica Nucleare, Sezione di Bari, I-70126 Bari, Italy*
[4]*State Key Laboratory of Particle Detection and Electronics, University of Science and Technology of China, Hefei 230026, China*
[5]*Department of Modern Physics, University of Science and Technology of China, Hefei 230026, China*
[6]*Department of Nuclear and Particle Physics, University of Geneva, Geneva CH-1211, Switzerland*
[7]*Dipartimento di Matematica e Fisica E. De Giorgi, Università del Salento, I-73100 Lecce, Italy*
[8]*Istituto Nazionale di Fisica Nucleare (INFN) - Sezione di Lecce, I-73100 Lecce, Italy*
[9]*University of Chinese Academy of Sciences, Beijing 100049, China*
[10]*Particle Astrophysics Division, Institute of High Energy Physics, Chinese Academy of Sciences, Beijing 100049, China*
[11]*Key Laboratory of Dark Matter and Space Astronomy, Purple Mountain Observatory, Chinese Academy of Sciences, Nanjing 210023, China*
[12]*School of Astronomy and Space Science, University of Science and Technology of China, Hefei 230026, China*
[13]*Istituto Nazionale di Fisica Nucleare (INFN)—Sezione di Perugia, I-06123 Perugia, Italy*
[14]*Institute of Modern Physics, Chinese Academy of Sciences, Lanzhou 730000, China*
[15]*National Space Science Center, Chinese Academy of Sciences, Beijing 100190, China*
[16]*Dipartimento di Fisica "M. Merlin" dell'Università e del Politecnico di Bari, I-70126 Bari, Italy*
[17]*Department of Physics and Laboratory for Space Research, the University of Hong Kong, Hong Kong SAR 999077, China*

(Received 18 May 2022; accepted 8 September 2022; published 29 September 2022)

[*]dampe@pmo.ac.cn
[†]Now at Istituto Nazionale Fisica Nucleare (INFN), Sezione di Napoli, IT-80126 Napoli, Italy.
[‡]Now at Università di Sassari, Dipartimento di Chimica e Farmacia, I-07100 Sassari, Italy.
[§]Also at Institute of Physics, Ecole Polytechnique Fédérale de Lausanne (EPFL), CH-1015 Lausanne, Switzerland.
[‖]Now at Dipartimento di Fisica e Chimica "E. Segrè", Università degli Studi di Palermo, I-90128 Palermo, Italy.
[¶]Also at School of Physics and Electronic Engineering, Linyi University, Linyi 276000, China.

More than a century after the performance of the oil drop experiment, the possible existence of fractionally charged particles (FCPs) still remains unsettled. The search for FCPs is crucial for some extensions of the Standard Model in particle physics. Most of the previously conducted searches for FCPs in cosmic rays were based on experiments underground or at high altitudes. However, there have been few searches for FCPs in cosmic rays carried out in orbit other than AMS-01 flown by a space shuttle and BESS by a balloon at the top of the atmosphere. In this study, we conduct an FCP search in space based on on-orbit data obtained using the Dark Matter Particle Explorer (DAMPE) satellite over a period of five years. Unlike underground experiments, which require an FCP energy of the order of hundreds of GeV, our FCP search starts at only a few GeV. An upper limit of 6.2×10^{-10} cm^{-2} sr^{-1} s^{-1} is obtained for the flux. Our results demonstrate that DAMPE exhibits higher sensitivity than experiments of similar types by three orders of magnitude that more stringently restricts the conditions for the existence of FCP in primary cosmic rays.

DOI: 10.1103/PhysRevD.106.063026

I. INTRODUCTION

The oil drop experiment originally performed by Robert A. Millikan in 1909 [1] provided the first direct measurement of the electric charge (e) of an electron. Since then, particles detected have been observed to carry charges that are integer multiples of e. It was believed that e is the smallest charge in nature until Gell-Mann and Zweig proposed the quark model in 1964 [2,3] that states quarks, as elementary particles, carry fractional charge values ($\frac{1}{3}e$ or $\frac{2}{3}e$). Thus, until theories of quantum chromodynamics (QCD) indicated that free quarks do not exist, research interest in fractionally charged particles (FCPs) was driven by the search for free quarks. However, benefitting from the development of new theories, FCPs are allowed in some extensions of the Standard Model (SM). For example, extensions of the SM gauge group SU(5) predict a color singlet particle with a charge of $\frac{1}{3}e$ [4,5]. In some larger groups, the existence of FCPs arises from a natural derivation [6–8]. Since then, this field of study has been oriented toward the search for any new fractionally charged particle.

FCPs are assumed to be a type of heavy lepton [9], that have a penetrating ability and are free from high energy cascade effects other than ionization and weak interactions. Over the last few decades, several experimental studies have been conducted to find counterexamples to the QCD assertion of the nonexistence of free quarks and to directly search for new particles with fractional charge. There are three primary methods to detect FCPs [10]. First, there is the modern Millikan oil drop technique that utilizes an oscillating electric field [11,12] to search for contained FCPs within the bulk matter on the earth. Second, high-energy accelerators are used to search for FCPs in the process of particles production to test superstring models or explore physics theories beyond the standard model [13–16]. Last, FCPs are also searched for in cosmic rays, and such a method can be subclassified into the following three types. (1) Ground-based experiments [17,18] are detecting cores of extensive air showers. In 1969, McCusker and Cairns claimed the discovery of a free $\frac{2}{3}e$ particle in a cloud chamber image [17] of an extensive air shower, however, no replication was ever achieved. (2) Underground experiments [19–24] evade background noise from extensive air showers and attempt to observe FCPs that pass through the overburden. Such FCPs would have to start out with an energy larger than hundreds of GeV to penetrate rocks before entering the underground laboratory. With a large acceptance and long exposure time, the underground experiment MACRO obtained a flux upper limit of 6.1×10^{-16} cm^{-2} sr^{-1} s^{-1} at the 90% confidence level (CL) [22] for particles with charges from $\frac{1}{4}e$ to $\frac{2}{3}e$. 3) Searches for FCPs in cosmic rays are also conducted in space, notably, on the space shuttle (AMS-01 [25]) and balloon (BESS [26]). Compared to underground experiments, particles with significantly lower energy in the order of a few GeV are able to be observed in space experiments where the stricter flux upper limit of 3.0×10^{-7} cm^{-2} sr^{-1} s^{-1} for FCPs was obtained from AMS-01. However, both the BESS and AMS-01 experiments were short-lived, and there has been no long-term continuous search for FCPs based on on-orbit experimentation.

II. DAMPE MISSION

The Dark Matter Particle Explorer (DAMPE [27,28], also known as "Wukong" in Chinese) is an on-orbit calorimetric-type, satellite-borne detector that can be used to search for FCPs in primary cosmic rays in space. One of the scientific objectives of DAMPE is to search for dark matter in an indirect approach that involves examining high-energy cosmic rays in space. Launched on 17 December 2015, the DAMPE detector has been in stable operation on the 500 km Sun-synchronous orbit for more than six years, and has made important contributions to the cosmic ray observation of electrons [29], protons [30], and helium [31]. From top to bottom, DAMPE consists of four sub-detectors as shown in Fig. 1. A Plastic scintillator detector (PSD) [32,33],

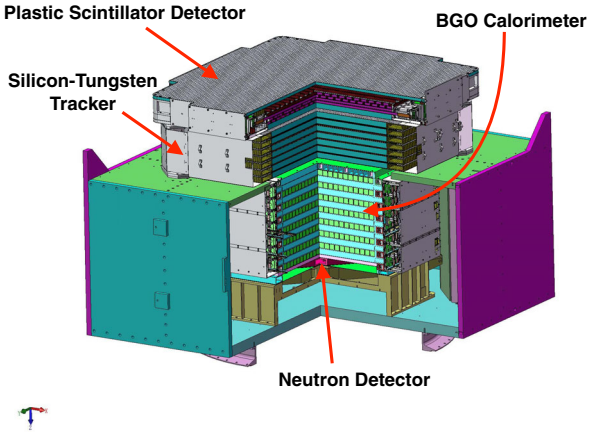

FIG. 1. The structure of the DAMPE detector.

that is made of two layers of 41 plastic scintillation strips. A Silicon-Tungsten tracker converter (STK) [34,35], that is composed of six modules of double-layer silicon-strip detectors, with three layers of tungsten inserted. A Bismuth Germanium Oxide (BGO) imaging calorimeter [36] consisting 14 layers of 22 crystal bars, corresponds to ∼32 radiation lengths and 1.6 nuclear interaction lengths. It also includes a Neutron Detector (NUD) [37], that is a collection of four boron-doped plastic scintillation tiles. The PSD measures the charge of the incident particle and contributes to the anticoincidence measurement of gamma rays. The STK reconstructs the trajectory and also measures the particle's charge. The BGO calorimeter measures the energy, provides particle identification, and provides the trigger for the DAMPE spectrometer. The NUD provides additional electron/hadron discrimination. The PSD strips and BGO crystals of DAMPE are arranged in parallel in each layer and orthogonally arranged between adjacent layers. The YOZ planes and XOZ planes are defined as lateral views perpendicular to the odd and even layers of the BGO calorimeter (numbered from 1 to 14), respectively.

DAMPE has good charge resolutions of $0.06e$ and $0.04e$ for measuring singly charged particles with the PSD [38] and STK [39], respectively. Furthermore, compared to similar types of space experiments, DAMPE has a relatively large acceptance and long exposure duration, which are advantageous in searching for FCPs. Here we conduct a search for FCPs based on on-orbit data collected with DAMPE over a period of five years.

III. DATA ANALYSIS

A. Target FCPs

The on-orbit data corresponding to the latitude region of $[-20°, +20°]$ is used to search for FCPs, where the strength of geomagnetic field is generally uniform, and the energy cutoff is usually ∼10 GeV for singly charged particles. Given that the acceleration mechanism of cosmic rays may be related to their charge [31], FCPs carry proportionately lower energy. Combined with the heavy lepton assumption, the search for FCPs is constrained to minimum ionizing particles (MIPs). While particles above the threshold primarily lie in the relativistic energy region, charge measurements using both PSD and STK are in approximate agreement with the Bethe-Bloch equation. Based on the measurements, the reconstructed charge value is the "key" information for the FCP detection. The measurement of energy deposition is expressed in units of the energy deposited by a singly charged MIP event, which deposits approximately 23 MeV in one BGO crystal [36]. Compared with a singly charged MIP event, the energy deposition of an FCP is proportional to the squared value of the particle's charge. The trigger system is generated by the BGO calorimeter, whose threshold for a MIP event is calibrated to be approximately $\frac{1}{5}$ MIP [40] based on on-orbit data. Thus, due to the very low trigger efficiency for FCPs with $\frac{1}{3}e$ ($\frac{1}{9}$ MIP), this study focuses on $\frac{2}{3}e$ FCPs.

B. Background estimation

Due to the limited charge resolution, high-energy protons/antiprotons, electrons/positrons, and high energy gamma rays are the primary sources of background noise. The BGO calorimeter is approximately 32 radiation lengths deep, thus excluding misidentifications caused by electrons/positrons and gamma rays. Moreover, the 1.6 nuclear interaction lengths deep such that 80% of protons/antiprotons develop hadronic showers; therefore, misidentification from the 20% nonshowering, MIP-like high-energy protons/antiprotons is the largest source of background.

C. Monte Carlo simulations

Monte Carlo (MC) simulations of protons and FCPs with $\frac{2}{3}e$ based on the GEANT4 [41] are used to study the background and signals. GEANT4 is capable of performing simulations on (virtual) particles with selected mass, charge, and physical process. Thus, we insert a virtual MIP-like FCP with $\frac{2}{3}e$ within the GEANT4 framework in the DAMPE software. Since the energy deposition of relativistic heavy leptonlike particles with a certain charge value is nearly independent of their masses, the mass of the FCP is arbitrarily taken to be 1200 MeV. The original index of the energy spectrum is taken to be −2.7, in agreement with the all-particle cosmic ray spectrum. The processes of multiple scattering and ionization are added. The sample of MC FCPs is used as the signal to be analyzed. Both primary and secondary protons are taken into account in evaluating the background.

D. Event selections

The MIP events are selected during the search for FCPs. The detailed event selection method is described below.

(i) *Trigger efficiency.* DAMPE comprises four trigger patterns [40]: unbiased trigger (UNBT), MIPs

trigger (MIPT), high energy trigger (HET), and low energy trigger (LET). The UNBT and MIPT are used in the event selection. The UNBT requires that the energy deposition of each of the first two BGO layers to be larger than $\frac{1}{5}$ MIP. The MIPT has two modes to select events that penetrate the BGO calorimeter from top to bottom. One requires the energy deposition of the layers 1, 11, 13 to be larger than $\frac{1}{5}$ MIP, while the other requires that of layers 2, 12, 14 to be larger than $\frac{1}{5}$ MIP. To reduce the amount of data storage, different prescale factors are applied independently to the UNBT, MIPT, and LET events during operation at different latitudes. UNBT has a relatively loose restriction and is used to estimate the efficiency of the other triggers.

Based on the on-orbit data, the MIPT is observed to be active only in the latitude range, $[-20°, +20°]$, where the prescale factors for MIPT and UNBT are $\frac{1}{4}$ and $\frac{1}{512}$, respectively. The trigger efficiency of on-orbit data requires the consideration of the pre-scale factors and is given by:

$$\epsilon_{\mathrm{MIPT}} = \frac{N_{\mathrm{MIPT}} \times 4}{N_{\mathrm{UNBT}} \times 512}, \tag{1}$$

where N_{MIPT} denotes the number of prescaled MIPT events, and N_{UNBT} is the number of prescaled UNBT events. The efficiency is observed to be generally steady at 97.3% as a function of time. No prescale factor is applied to the MC sample, and the trigger efficiencies for MC protons and FCPs of $\frac{2}{3}e$ are 99.4% and 85.5%, respectively.

(ii) *Track selection.* BGO tracks are reconstructed for each event passing through the BGO calorimeter. Ideally, the BGO track is required to be completely contained within the detector while implementing a geometric selection. Moreover, coincidence of the track with the edges of the first layer of PSD strips or the edges of the last layer of BGO crystals are excluded. Then, a satisfactory track reconstruction using the STK with the track seed provided by the BGO is required [42]. In order to evaluate the track efficiency, a sample is selected based on the BGO track, and the efficiency is estimated from the fraction of the sample selected using the STK track. Thus, the track efficiency is given by

$$\epsilon_{\mathrm{track}} = \frac{N_{\mathrm{STK\&BGO}}}{N_{\mathrm{BGO}}}, \tag{2}$$

where N_{BGO} denotes the number of events selected with the BGO track and $N_{\mathrm{STK\&BGO}}$ is the number of further events corresponding to the STK track.

Considering the large size (25 mm × 25 mm × 600 mm) of each BGO crystal, the reconstruction of a BGO track has a relatively large uncertainty. The angle difference between the BGO track and STK track is restricted in order to eliminate scattering events and enhance the reliability of the STK track. As depicted in Fig. 2, the distributions of the angle difference between the on-orbit data and MC protons exhibit good agreement in $[-4°, +4°]$ in both the YOZ and XOZ planes. The discrepancy between the MC proton and on-orbit data in the region of larger angles can be attributed to multiple scattering.

(iii) *MIP requirements.* To purify the MIP events, the respective MIP requirements are applied to the PSD and the BGO. Besides the fired PSD strip and BGO crystal, some events may be oblique injections through adjacent cells of strips or crystals, or generating knock-on electrons. In such cases, multiple fired cells appear on the PSD and BGO layers. Thus, a relatively loose limit of 2 strips and 2 crystals per layer is applied to aid the selection of MIP events. In the PSD, at most two fired strips are allowed in each layer. Since the energy fluctuations

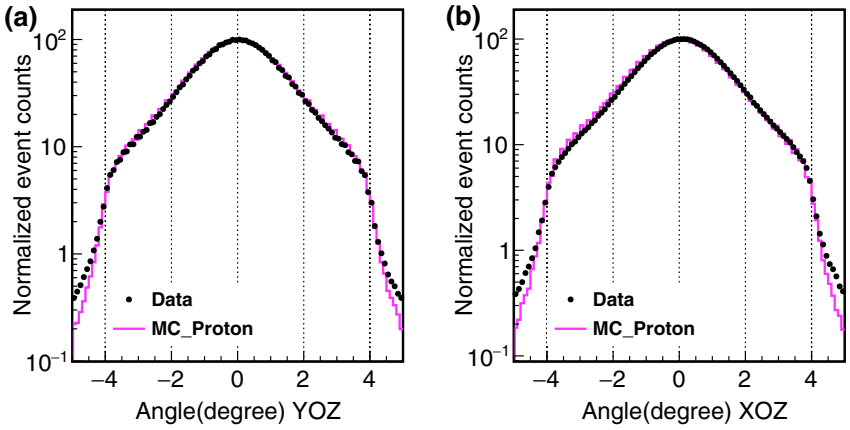

FIG. 2. The angle difference between the BGO track and STK track. The (a) and (b) panels depict the distributions of angle difference in the YOZ and XOZ planes, respectively. The angle differences obtained from the on-orbit data (black dots) and MC proton (pink solid line) agree well within $[-4°, +4°]$.

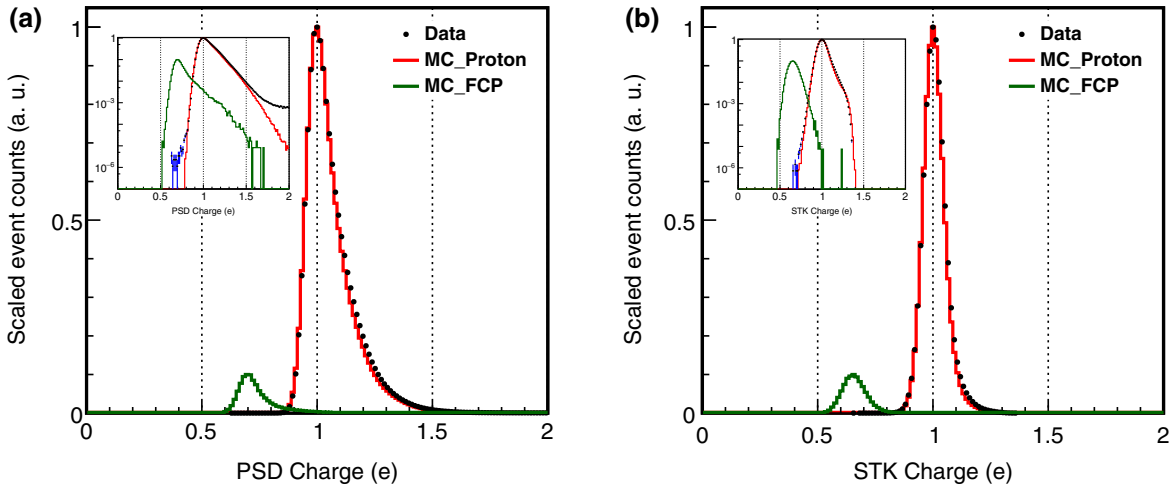

FIG. 3. The distributions of charges measured by the PSD (a) and STK (b). The spectra obtained from on-orbit data (black dots) and MC protons (red line) are normalized with ordinate values in arbitrary units and are consistent. The FCP (green line) is well distinguished from singly charged particles. The log scale distributions for the PSD and STK are shown in the insets.

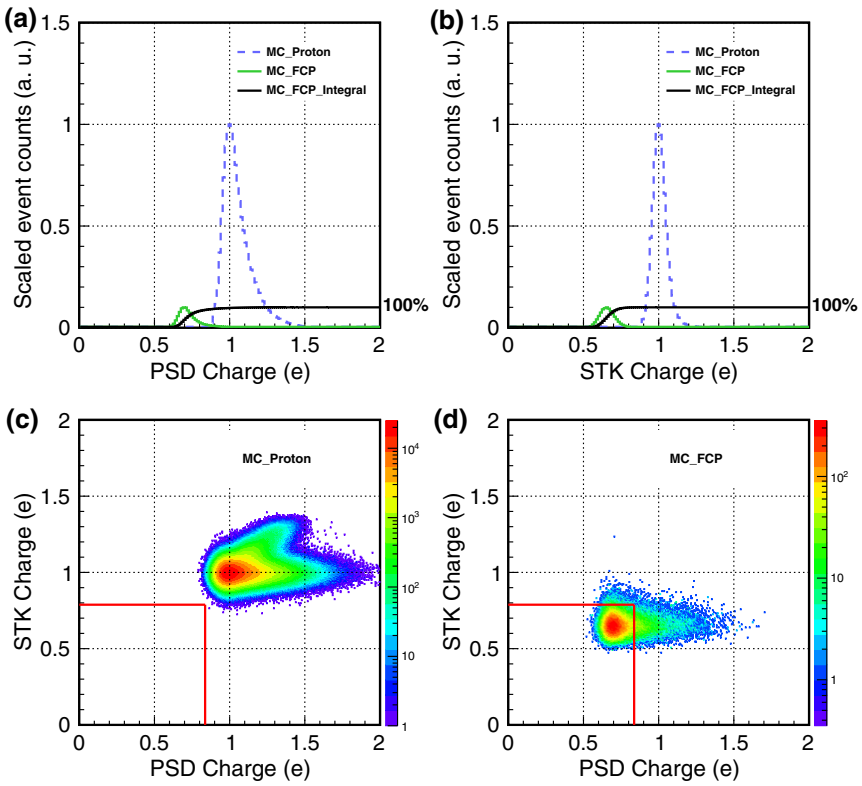

FIG. 4. The charge distributions from the PSD and STK and the definition of the signal region. The charge distributions for the PSD and STK are shown in panels (a) and (b), respectively. The event counts are scaled to arbitrary units. The solid green lines correspond to MC FCPs and the dashed blue lines are for MC protons. With the help of the integrals of FCP charges represented by the solid black lines, the signal region is defined based on the distributions presented in panels (a) and (b). The red lines in panels (c) and (d) represent the signal region for FCPs where the charge values for the PSD and STK are $0.84e$ and $0.79e$, respectively. All background proton MIP events fall outside the region, as depicted in panel (c). Injections from the bottom surface to the top surface of DAMPE are simulated and excluded as well. The combined efficiency of the signal region for FCPs is approximately 86.0%, as depicted in panel (d).

induced by each event passing through a corner of the PSD strip significantly affect the charge reconstruction, the fired strips are required to be penetrated by the trajectories from the top surface to the bottom surface. Similarly, in the BGO calorimeter, at most two fired crystals are allowed in each layer and more than ten layers of the BGO are required to have signals. Moreover, at least one of the final two layers (13 or 14) of the BGO is required to have a signal to ensure the full penetration through the BGO calorimeter.

(iv) *Charge reconstruction.* Signals from both ends of a fired PSD strip should be consistent within the fluorescence attenuation correction. To ensure the reliability of charge reconstruction, the ratio of charge values at the two ends of the PSD strip is constrained. The average value of two PSD layers is taken to be the PSD charge. The STK charge is also taken to be the average of the charge values corresponding to multiple layers after correction [39]. The results of charge reconstruction are depicted in Fig. 3. MC FCPs and singly charged MIPs are adequately distinguishable in both the PSD and STK. The charge spectra obtained from the on-orbit data and MC protons display close similarity.

E. Definition of the signal region

The differences in the charge distributions between MC protons and MC FCPs are depicted in Fig. 4(a) and 4(b). The integrals of MC FCPs are also drawn in the corresponding panel to evaluate the selection of the signal region. The signal region is defined as the area where the charge values of the PSD and STK are less than $0.84e$ and $0.79e$, respectively. The standard deviation σ is obtained by dividing the full width at half maximum of the distributions by 2.35. The values corresponding to the signal region are obtained by adding 3σ to the peak value. The two-dimensional distributions of the PSD-STK charges of MC samples are depicted in Fig. 4(c) and 4(d) accompanied by the signal region indicated by red lines. A combined integral efficiency of the signal region of up to 86% is observed for MC FCPs, as shown in Fig. 4(d). The signal region is deemed to be adequate for excluding the background from proton MIP events, as depicted in Fig. 4(c).

Figure 5 shows the two-dimensional PSD-STK charge distribution of the on-orbit data, as well as the signal region that is shown as the red lines.

IV. RESULTS

The flux of $\frac{2}{3}e$ FCPs is given by Eq. (3)

$$\Phi = \frac{N_{\rm obs}}{T_{\rm exp}\epsilon_{\rm scale}\epsilon_{\rm trig}A_{\rm eff}\epsilon_{\rm region}}, \tag{3}$$

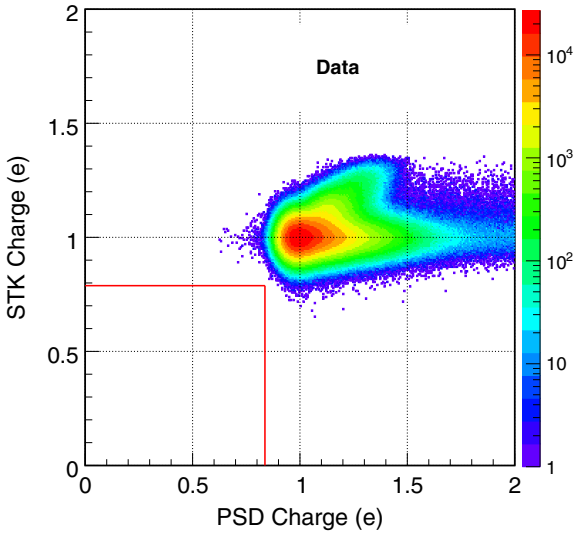

FIG. 5. The distribution of PSD-STK charge for on-orbit data. The red lines indicate the signal region for FCPs. The signal region is defined to cover candidate FCP event, while rejecting the proton background. No candidate event is observed to lie within the signal region. The portion above 1.1e of both PSD and STK charges corresponds to the events that inject from the bottom to the top of DAMPE. These events are low-energy secondary particles of extensive air showers.

where $T_{\rm exp}$ denotes the effective exposure time for this work, $\epsilon_{\rm scale}$ the prescale factor of MIPT, $\epsilon_{\rm trig}$ the efficiency of the MIPT for FCPs, $A_{\rm eff}$ the effective acceptance for FCPs, $\epsilon_{\rm region}$ the efficiency of the signal region for FCPs, and $N_{\rm obs}$ the number of observed FCPs candidates. The results reported in this work are based on data recorded from 01.01.2016 to 12.31.2020. The data are sampled from the latitude range, $[-20°, +20°]$, where the $T_{\rm exp}$ is equal to approximately 2.34×10^7 s, followed by the deduction of the dead time of the detection system as well as the time when the satellite was in the South Atlantic Anomaly region. The MIPT pattern is used in this analysis, which relies on simultaneous signals in the upper and lower layers of the BGO calorimeter. $\epsilon_{\rm scale} = \frac{1}{4}$ is designed for MIPT and $\epsilon_{\rm trig} = 85.5\%$ is based on FCP simulations. $A_{\rm eff}$ for FCP is also estimated based on the MC sample as $A_{\rm eff} = A_{\rm geo} \times \epsilon_{\rm sel}$, where $A_{\rm geo}$ denotes the geometric acceptance, and is approximately equal to 3000 $\rm cm^{-2}$ sr, and $\epsilon_{\rm sel}$ denotes the total selection efficiency, which depends on the selection method. $A_{\rm eff} = 940$ $\rm cm^{-2}$ sr is observed following the selection process. $\epsilon_{\rm region}$ represents the efficiency of the signal region for FCPs and is evaluated to be 86%. Since no candidate event is observed within the signal region and the amount of background is negligible, for the upper limit, $N_{\rm obs}$ is taken to be 2.44 at the 90% CL [43].

We assume that the systematic uncertainties of FCPs are the same as those of singly charged MIP events. The combined systematic uncertainty δ includes the effects of trigger efficiency, track reconstruction, and the detection

TABLE I. The comparison between DAMPE and other similar types experiments.

Experiments	Geometric acceptance(cm^{-2} sr)	Exposure time (s)	Upper limit (cm^{-2} sr^{-1} s^{-1})
AMS-01	3000	3.6×10^4	3.0×10^{-7} (95% CL)
BESS	1500	3.2×10^5	4.5×10^{-7} (90% CL)
DAMPE	3000	2.3×10^7	6.2×10^{-10} (90% CL)

efficiency of the PSD and STK. The systematic uncertainties are investigated in the selection procedure based on comparisons between the MC proton and on-orbit data. A half of the differences between the efficiencies corresponding to on-orbit data and MC protons are considered as systematic uncertainties. The total systematic uncertainty of the selections is given by

$$\delta = \sqrt{\delta^2_{\text{trigger}} + \delta^2_{\text{track}} + \delta^2_{\text{charge}}}, \tag{4}$$

where $\delta_{\text{trigger}} = 1.1\%$, $\delta_{\text{track}} = 2.9\%$, and $\delta_{\text{charge}} = 0.5\%$ denote the corresponding systematic uncertainties of the trigger, track selection, and charge selection efficiencies, respectively. Systematic uncertainties corresponding to other very loose selections are negligible, where the total uncertainty is 3.1%.

With systematic uncertainties considered, the flux upper limit of $\frac{2}{3}e$ FCP is found to be $\Phi < 6.2 \times 10^{-10} \text{cm}^{-2}\,\text{sr}^{-1}\,\text{s}^{-1}$.

Table I presents the complete results and some vital parameters of DAMPE, compared with other similar experiments. Figure 6 shows the upper limits from other FCP searches. Among underground experiments, MACRO yields the most sensitive upper limit. The CDMS II and MAJORANA experiments have high degrees of sensitivity to small charges because of the lower thresholds of the respective detection systems. Among space equipment, AMS-01 has a large geometric acceptance [44], but a short exposure duration. BESS integrates data gathered over four flights to achieve a longer exposure time but its geometric acceptance is limited. DAMPE has the longest and continuous exposure time as well as relatively large geometric acceptance, and therefore it yields the most stringent FCP flux upper limit for space experiments,in space, with an improvement of three orders of magnitude over previous work.

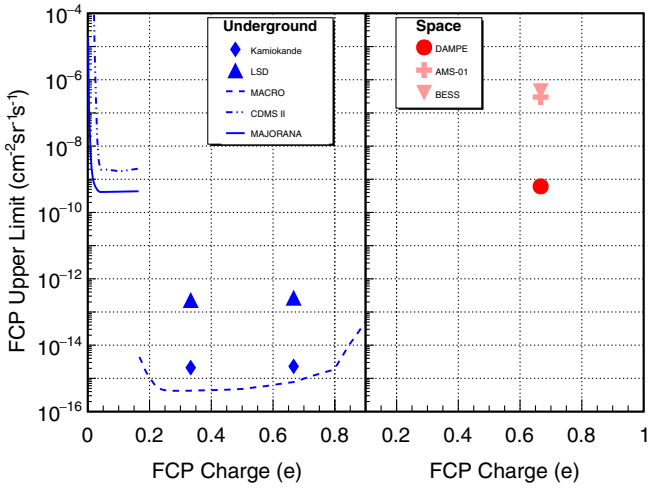

FIG. 6. FCP ux upper limit versus electric charge from different cosmic ray experiments. The results of underground experiments which require the particles to have energy above ~100s GeV are shown in the left panel. The results of space experiments which detect the particles above a few GeV due to the limitation of geomagnetic cuto are shown in the right panel. The DAMPE upper limit (red dot) is lower than those from AMS-01 [25] (light red cross) and BESS [26] (red inverted triangle). The results of the underground experiments such as LSD [20] (blue triangles), Kamiokande II [19] (blue full diamond), MACRO [21] (blue dashed line), CDMS II [23] (blue dotted line), and MAJORANA [24] (blue solid line) are shown also.

V. SUMMARY

Based on on-orbit data obtained from DAMPE over a period of five years the results of the search for $\frac{2}{3}e$ FCPs in primary cosmic rays are as follows. No FCP signals are observed and a flux upper limit of $\Phi < 6.2 \times 10^{-10}$ $\text{cm}^{-2}\,\text{sr}^{-1}\,\text{s}^{-1}$ is established at the 90% CL A precise measurement of the flux or a conservative flux upper limit is essential to construct and constrain the model of FCPs. Most of the previously performed underground experiments assumed that FCPs would exhibit long penetration paths, which, in turn, requires them to have energy exceeding a few hundred GeV. Given the effective energy threshold arising from the geometric cutoff, experiments in space can be used to detect FCPs with energy as low as a few GeV. DAMPE serves as a novel observation platform and enables a long-term, continuous search for relatively low-energy FCPs in primary cosmic rays. In the future, with the accumulation of more on-orbit data, DAMPE is expected to perform even more sensitive FCP searches.

ACKNOWLEDGMENTS

We acknowledge Prof. Xiaowei Tang and Prof. Zhengguo Zhao for their suggestions and encouragement for this work. We also thank Mr. Wilson J. Huang for proofreading the manuscript. The DAMPE mission was funded by the strategic priority science and technology projects in space science of Chinese Academy of Sciences. In China the data analysis is supported by the National Key Research and Development Program of China (No. 2016YFA0400200), the National Natural Science

Foundation of China (No. 11673021, No. U1738205, No. U1738208, No. U1738139, No. U1738135, No. 11705197, No. 11851302), the strategic priority science and technology projects of Chinese Academy of Sciences (No. XDA15051100), the Youth Innovation Promotion Association CAS (Grant No. 2021450), the Outstanding Youth Science Foundation of NSFC (No. 12022503), the CAS Project for Young Scientists in Basic Research (No. YSBR-061). In Europe the activities and data analysis are supported by the Swiss National Science Foundation (SNSF), Switzerland, the National Institute for Nuclear Physics (INFN), Italy, and the European Research Council (ERC) under the European Union's Horizon 2020 research and innovation programme (No. 851103).

[1] R. A. Millikan, Phys. Rev. **29**, 560 (1909).
[2] M. Gell-Mann, Phys. Lett. **8**, 214 (1964).
[3] G. Zweig, Tech. Rep., CM-P00042884, 1964.
[4] P. H. Frampton and T. W. Kephart, Phys. Rev. Lett. **49**, 1310 (1982).
[5] S. M. Barr, D. B. Reiss, and A. Zee, Phys. Rev. Lett. **50**, 317 (1983).
[6] H. W. Yu, Phys. Lett. **142B**, 42 (1984).
[7] K. Yamamoto, Phys. Lett. **120B**, 157 (1983).
[8] F. Dong, T. Tu, P. Xue, and X. Zhou, Phys. Lett. **129B**, 405 (1983).
[9] P. Langacker and G. Steigman, Phys. Rev. D **84**, 065040 (2011).
[10] M. L. Perl *et al.*, Mod. Phys. Lett. **19**, 2595 (2004).
[11] P. F. Smith, Annu. Rev. Nucl. Part. Sci. **39**, 73 (1989).
[12] V. Halyo, P. Kim, E. R. Lee, I. T. Lee, D. Loomba, and M. L. Perl, Phys. Rev. Lett. **84**, 2576 (2000).
[13] L. Lyons *et al.*, Z. Phys. C Part. Fields **36**, 363 (1987).
[14] S. Cecchini, H. Dekhissi, G. Giacomelli, G. Mandrioli, A. R. Margiotta, L. Patrizii, F. Predieri, P. Serra, and M. Spurio, Astropart. Phys. **1**, 369 (1993).
[15] L. W. Jones, Rev. Mod. Phys. **49**, 717 (1977).
[16] S. Chatrchyan *et al.*, Phys. Rev. D **87**, 092008 (2013).
[17] C. B. A. McCusker and I. Cairns, Phys. Rev. Lett. **23**, 658 (1969).
[18] H. Tang *et al.*, Chin. Phys. C **6**, 520 (1982).
[19] M. Mori *et al.*, Phys. Rev. D **43**, 2843 (1991).
[20] M. Aglietta *et al.*, Astropart. Phys. **2**, 29 (1994).
[21] M. Ambrosio *et al.*, Phys. Rev. D **62**, 052003 (2000).
[22] M. Ambrosio *et al.*, arXiv:hep-ex/0402006.
[23] R. Agnese *et al.*, Phys. Rev. Lett. **114**, 111302 (2015).
[24] S. I. Alvis *et al.*, Phys. Rev. Lett. **120**, 211804 (2018).
[25] C. Sbarra *et al.*, arXiv:astro-ph/0304192.
[26] H. Fuke *et al.*, Adv. Space Res. **41**, 2050 (2008).
[27] J. Chang *et al.*, Astropart. Phys. **95**, 6 (2017).
[28] G. Ambrosi *et al.*, Astropart. Phys. **106**, 18 (2019).
[29] G. Ambrosi *et al.*, Nature (London) **552**, 63 (2017).
[30] Q. An *et al.*, Sci. Adv. **5**, eaax3793 (2019).
[31] F. Alemanno *et al.*, Phys. Rev. Lett. **126**, 201102 (2021).
[32] Y. Yu *et al.*, Astropart. Phys. **94**, 1 (2017).
[33] P. Ma *et al.*, Res. Astron. Astrophys. **19**, 082 (2019).
[34] P. Azzarello *et al.*, Nucl. Instrum. Methods Phys. Res., Sect. A **831**, 378 (2016).
[35] A. Tykhonov *et al.*, Nucl. Instrum. Methods Phys. Res., Sect. A **893**, 43 (2018).
[36] Z. Zhang *et al.*, Nucl. Instrum. Methods Phys. Res., Sect. A **836**, 98 (2016).
[37] Y. Huang, T. Ma, C. Yue, Y. Zhang, M. Cai, J. Chang, T. Dong, and Y. Zhang, Res. Astron. Astrophys. **20**, 153 (2020).
[38] T. Dong *et al.*, Astropart. Phys. **105**, 31 (2019).
[39] S. Vitillo *et al.*, *Proc. Sci.*, 301 (2017) 240.
[40] Y. Zhang, J. Guo, Y. Liu, C. Feng, Y. Zhang, T. Dong, J. Zang, and C. Yue, Res. Astron. Astrophys. **19**, 123 (2019).
[41] S. Agostinelli *et al.*, Nucl. Instrum. Methods Phys. Res., Sect. A **506**, 250 (2003).
[42] A. Tykhonov, V. Gallo, X. Wu, and S. Zimmer, J. Phys. **898**, 042031 (2017).
[43] G. J. Feldman and R. D. Cousins, Phys. Rev. D **57**, 3873 (1998).
[44] J. Alcaraz *et al.*, Phys. Lett. B **461**, 387 (1999).